15. Simple boundary element models using the average slip in the two main patches of the finite fault model produce a pattern of localized uplift in the region of convergence between the two slip domains that is >30% larger than at comparable distances from the trench along-strike. The lack of uplift and other slip observations away from the exposed islands preclude more detailed modeling at present.
16. A. M. Dziewonski, D. L. Anderson, *Phys. Earth Planet. Inter.* **25**, 297 (1981).
17. P. Tregoning *et al.*, *J. Geophys. Res.* **103**, 12181 (1998).
18. The directivity parameter, $\Gamma = \cos(\phi_{sta} - \phi_{rup})/c$, where ϕ_{sta} is the station azimuth, ϕ_{rup} is a unilateral rupture azimuth, and c is a reference phase velocity [c is chosen as 4.0 km/s, the phase velocity for 80-s-period Rayleigh waves for model PREM (*16*)].
19. The Incorporated Research Institutions for Seismology data management center provided the broadband seismic data. We thank C. Biryol and S. L. Beck for sharing a preprint manuscript and H. Kanamori for discussions about surface wave STFs and slip inversions. This work was supported in part by NSF under grant EAR0635570 (T.L.). We thank three anonymous reviewers for comments on the manuscript.

Supporting Online Material

www.sciencemag.org/cgi/content/full/324/5924/226/DC1
Methods
Figs. S1 to S11
Table S1
References

21 October 2008; accepted 26 February 2009
10.1126/science.1167476

Curved Plasma Channel Generation Using Ultraintense Airy Beams

Pavel Polynkin,[1]* Miroslav Kolesik,[1] Jerome V. Moloney,[1,2] Georgios A. Siviloglou,[3] Demetrios N. Christodoulides[3]

Plasma channel generation (or filamentation) using ultraintense laser pulses in dielectric media has a wide spectrum of applications, ranging from remote sensing to terahertz generation to lightning control. So far, laser filamentation has been triggered with the use of ultrafast pulses with axially symmetric spatial beam profiles, thereby generating straight filaments. We report the experimental observation of curved plasma channels generated in air using femtosecond Airy beams. In this unusual propagation regime, the tightly confined main intensity feature of the axially nonsymmetric laser beam propagates along a bent trajectory, leaving a curved plasma channel behind. Secondary channels bifurcate from the primary bent channel at several locations along the beam path. The broadband radiation emanating from different longitudinal sections of the curved filament propagates along angularly resolved trajectories.

The initial observation of plasma channel generation by intense femtosecond laser pulses in air (*1*) paved the way for a series of fundamental studies in the field of extreme nonlinear optics of gaseous media. Continued interest in the subject is fueled by various potential applications such as remote spectroscopy (*2*), generation of terahertz waves (*3*, *4*), compression of ultrashort laser pulses down to few optical cycles (*5*), and atmospheric science (*6*).

During propagation of an ultraintense and ultrashort laser pulse in a transparent gaseous medium, the defocusing effect of the plasma generated via multiphoton ionization prevents the beam from the self-focusing collapse to a singularity. The hot core of the beam, composed of the high-intensity laser field and the generated plasma, is referred to as the filament. Filaments are typically ~100 μm in diameter and exhibit self-guided, subdiffractive propagation over long distances (*7*–*9*).

One of the important attributes of laser-induced filaments is the forward emission of broadband light, the very property that enables various remote-spectroscopy applications (*2*). This so-called conical emission carries information concerning pulse dynamics, which can be deduced by analyzing the associated angularly resolved spectra in the far field (*10*).

In early studies of femtosecond laser filamentation initiated by ultrashort pulses with Gaussian (*1*) or flat-top (*11*) spatial beam profiles or more complex waveforms such as Bessel (*12*, *13*) and hollow ring beams (*14*), the beams were axially symmetric. Consequently, the plasma channels were always generated along straight lines. Analysis of the conical radiation emanating from straight filaments is complicated by the fact that emissions originating from different longitudinal sections of the beam overlap in the observation plane.

In this study, we used femtosecond pulses with the transverse spatial beam profile in the form of a two-dimensional (2D) Airy function, the so-called Airy beams (*15*, *16*), for the initiation of filamentation. Generation of Airy beams relies on the fact that the Airy function $\mathrm{Ai}(x/x_0)$ and the complex exponential $\exp[i(\beta K)^3/3]$ form a Fourier transform pair, where x and K are conjugate variables and x_0 and β are appropriate scale factors. Thus a plane wave can be converted into an Airy beam by applying a cubic phase modulation followed by a spatial Fourier transformation through focusing with a lens (*15*). Airy beams are not axially symmetric and exhibit the following two unusual characteristics: (i) They remain approximately diffraction-free. (ii) Their main intensity features tend to freely self-bend (or transversely accelerate) during propagation (*15*–*18*). In fact, these beams follow parabolic trajectories in a way analogous to the ballistics of projectiles moving under the action of gravity (*17*). On the other hand, the "center of gravity" of an Airy beam moves along a straight path, in agreement with Ehrenfest's momentum theorem (*17*, *19*). In principle, Airy wave packets can be synthesized simultaneously in both space and time resulting in nondispersive and spatially localized temporal waves or optical bullets that are impervious to both dispersion and diffraction (*16*, *20*).

When intense femtosecond Airy beams are used for initiation of the filamentation, an unusual propagation regime results, in which the binding strength between the filamented beam core and its remaining quasi-linear part can be manipulated by varying the transverse acceleration of the Airy pattern. The generated plasma channel is curved,

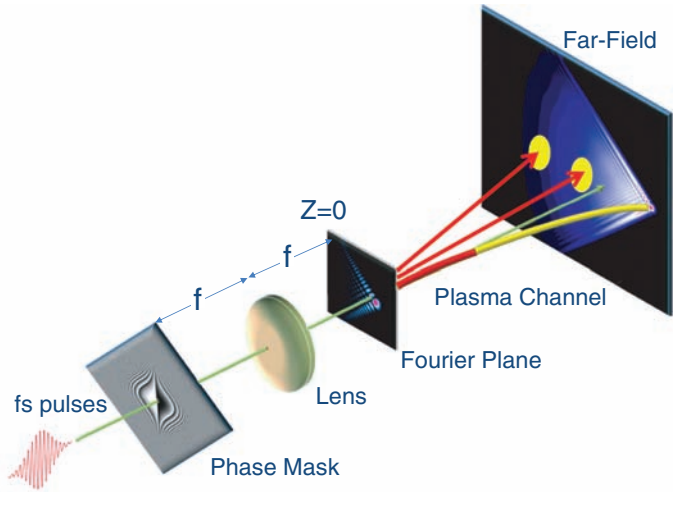

Fig. 1. Experimental setup. The continuous wave visible laser beam that we used as a spatial reference has a much smaller size than that of the phase mask. The reference beam experiences a negligible wavefront modulation and propagates along a straight line.

[1]College of Optical Sciences, University of Arizona, Tucson, AZ 85721, USA. [2]Department of Mathematics, University of Arizona, Tucson, AZ 85721, USA. [3]Center for Research and Education in Optics and Lasers–College of Optics and Photonics, University of Central Florida, Orlando, FL 32816, USA.

*To whom correspondence should be addressed. E-mail: ppolynkin@optics.arizona.edu

and such an arrangement acts as a streak camera by projecting the broadband emission from different longitudinal sections of the filament along angularly separated paths, resulting in the spatial separation of this emission in the far field.

In the experimental setup (Fig. 1), 35-fs laser pulses are generated by a multistage Ti:sapphire system having a clean Gaussian spatial mode profile. The laser output is passed through a transparent phase mask that imposes a 2D cubic phase pattern onto the beam. This wavefront is subsequently focused, and the spatial Fourier image of the field is formed at the focal plane of the lens. The transverse dimension of the resulting Airy beam can be scaled, and the corresponding acceleration can be varied with lenses that have different focal lengths.

To simulate beam propagation numerically, we used a pulse propagator code based on the unidirectional pulse propagation equation (*21*). The model used accounts for linear diffraction, group velocity dispersion, and Kerr effect, as well as for plasma generation via multiphoton ionization and the associated beam defocusing.

The experimentally measured parabolic trajectory of the dominant intensity feature of the beam is shown for two different focusing lenses (Fig. 2A). The beam deflection with respect to a straight reference beam propagating along the optical axis is plotted as a function of the propagation distance. From the scaling properties of Airy beams, the lens with shorter focal length yields a faster self-deflection rate (as expected), and the ratio of these two accelerations is approximately equal to the inverse ratio of the two focal lengths cubed.

We consider only the $f = 75$ cm case (here, f is the focal length of the lens) where the transverse acceleration is more pronounced. The plasma density along the beam path was measured by a capacitor-based plasma probe (*12*) with a longitudinal resolution of 5 mm (Fig. 2B). It is evident that the generated plasma channel remains longitudinally continuous (within the spatial resolution of the probe) for all three values of the pulse energy. The plasma channel starts to form before the Fourier plane, and the length of the channel grows with increasing pulse energy. For comparison, the plasma density generated from the filamentation of the corresponding Gaussian beam (when the phase mask is removed) is also shown. In this latter case, the generated plasma is more dense, but the plasma channel is shorter compared to that generated

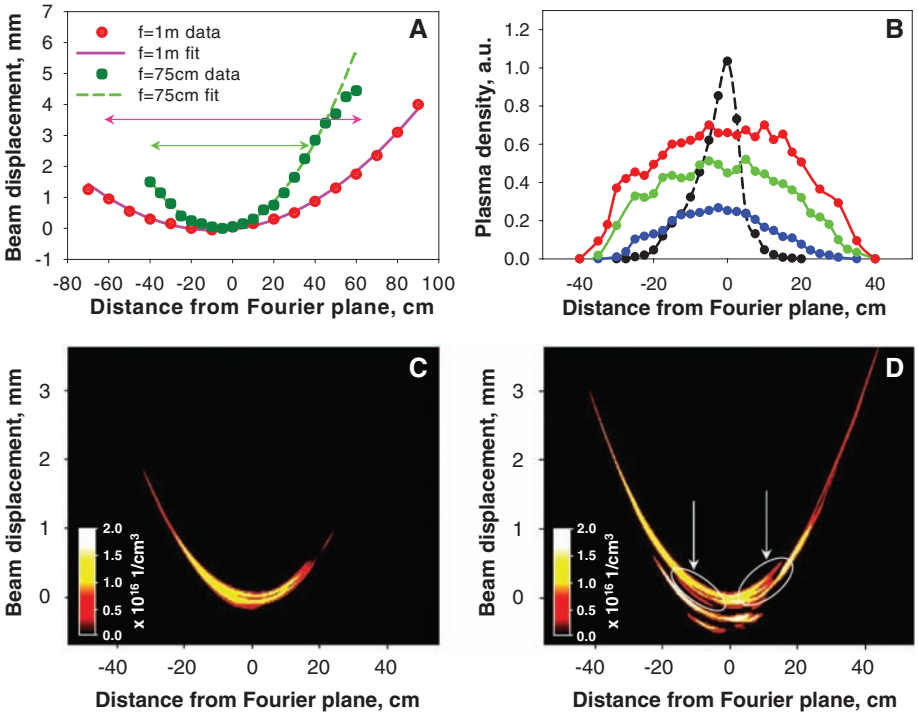

Fig. 2. (**A**) Deflection of a femtosecond Airy beam with 5-mJ pulse energy for two different focusing lenses with focal lengths equal to 75 cm and 1 m. Fitting the data with parabolas yields the beam acceleration parameters 1.3×10^{-3} mm/cm^2 and 4.0×10^{-4} mm/cm^2 for lenses with $f = 75$ cm and 1 m, respectively. Horizontal arrows show the approximate extent of the generated plasma channels in these two cases. (**B**) Linear plasma density along the filament for $f = 75$ cm focusing and different pulse energies: 5 mJ (blue), 10 mJ (green), and 15 mJ (red). The black dashed curve shows plasma density (scaled down by a factor of 3) with the phase mask removed at 10-mJ pulse energy. (**C**) Results of numerical simulations for the peak free-electron density in plane of curvature of the Airy beam for 5-mJ pulses. The generated plasma channel is continuous and smooth. (**D**) Same as in (C) but for 10-mJ pulses. Secondary lobes of the Airy beam start generating their own plasma channels, and the main channel develops bifurcations along the propagation path. Locations of the two most pronounced bifurcations are indicated with arrows.

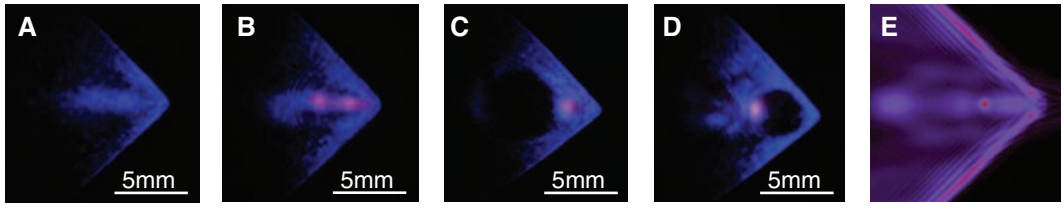

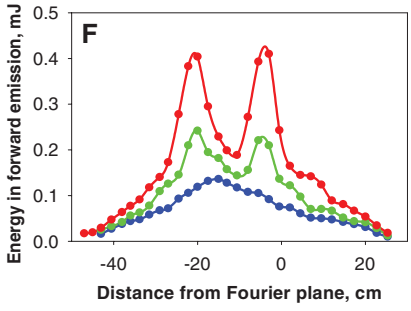

Fig. 3. (**A** to **D**) Photographs of the far-field emission patterns at different pulse energies. The forward emission pattern is elliptical for 5-mJ pulses (A) and breaks into two spots for higher-energy pulses [10 mJ, (B)]. Each of the two spots can be selectively blocked by masking the tip of the Airy beam at $z = -20$ cm (C) and $z = 0$ (D). (**E**) Numerically simulated far-field emission pattern for 10-mJ pulses showing breakup of the forward emission into multiple isolated spots. (**F**) Intensity distribution of the forward emission along the filament, for different values of pulse energy: 5 mJ (blue), 7.5 mJ (green), and 10 mJ (red). At energies above 5 mJ, the distribution develops two peaks that are consistent with two spots in the photographs of emission patterns.

by an Airy beam of the same transverse size and pulse energy. The generation of extended filaments by Airy beams is a direct consequence of their diffraction-free nature.

In Fig. 2, C and D, we show simulation results for the plasma density generated by the accelerating beam for different values of pulse energy. The color-coded plots show the peak free electron density in the plane of the curved laser beam. According to these simulations, above a certain pulse-energy threshold, the continuous curved plasma channel develops bifurcations or split-off channels. The locations of these bifurcations are indicated by white arrows in Fig. 2D. The split-off channels do not extend far and die out without the support of the accelerating beam. In addition, at high energies, the secondary lobes of the Airy beam generate their own local plasma channels that are weaker and shorter than the primary channel generated by the dominant lobe of the beam.

According to the dynamic spatial replenishment theory (*7*), the length of a plasma channel approximately scales with the extent of the linear focus zone of the laser beam. For Airy beams generated from Gaussian beams via cubic phase modulation and focusing, the distance from the focal plane of the lens over which the peak intensity drops to the exp(–2) level can be estimated by $z_0 \approx 2.8\,\Phi_{tot}^{1/3} W_A^2/\lambda$, where Φ_{tot} is the total phase imposed by the cubic phase mask across the full exp(–2) intensity width of the incident Gaussian beam, W_A is the full width at half maximum (FWHM) of the main lobe of the generated Airy pattern at the focal plane of the lens, and λ is the optical wavelength (*22*). The length of the generated plasma channel can be roughly estimated as twice this distance ($2z_0$). The transverse deflection Δ of the dominant lobe of the beam as a function of distance z is approximately described by $\Delta(z) = 0.037\,\lambda^2 z^2/W_A^3$. In the experiment, $\Phi_{tot} \approx 180$ rad, $W_A = 132$ μm, and the center wavelength of the laser source is 0.8 μm. With these parameters, the total length of the generated plasma channel is estimated to be $2z_0 \approx 69$ cm, and in this case the beam acceleration rate is $\Delta(z)/z^2 \approx 1.04 \times 10^{-3}$ mm/cm^2. These values are in good agreement with the experimental data and simulations shown in Fig. 2. Note that an equivalent Gaussian beam with FWHM equal to W_A would decay to the exp(–2) level, due to diffraction, after propagating a distance of about one third of z_0.

Photographs of the beam along with the forward emission from the generated filament (Fig. 3, A to D) were taken on a weakly fluorescent screen placed 50 cm away from the Fourier plane, shortly after the plasma channel ceased. At this distance, the beam pattern differs substantially from a 2D Airy function because of both the finite beam size and distortions resulting from filamentation. The forward emission from different longitudinal segments of the filament is spatially resolved along the horizontal direction. At a low pulse energy (5 mJ; Fig. 3A), the pattern of emission is a horizontal ellipse, indicative of a continuous bent plasma channel. As the energy is increased (10 mJ; Fig. 3B), the far-field emission pattern breaks into two spots. Because of the self-healing properties of Airy beams (*23*, *24*), each spot can be selectively blocked without affecting the other one by masking the tip of the Airy pattern at an appropriate location along the propagation direction. In other words, the Airy pattern can regenerate itself during propagation, even if a portion of it has been blocked.

Numerical simulations qualitatively reproduce the observed emission pattern broken into multiple spots at high pulse energies (Fig. 3E).

The energy distribution of the forward emission by the filament (Fig. 3F) was recorded by measuring the pulse energy passing through a 5-mm circular aperture placed 3 m after the Fourier plane. The aperture's position is traced to the exact location along the plasma channel from which the forward emission originated, as schematically shown in Fig. 1. What facilitates this mapping is the fact that the light beam and the associated plasma channel self-bend along a predictable trajectory. The transition from the continuous emission at low pulse energies to the lumped emission into well-defined spots at high energies is evident. This type of diagnostics is impossible with standard axially symmetric optical beams (producing straight plasma channels) because the emissions from different longitudinal sections of the filament would overlap in the far field.

The data shown in Fig. 3F is consistent with the results of the plasma-density simulations that show the formation of two secondary filaments that branch out from the primary filament at high pulse energy. These split-off filaments leave their marks in the spatially resolved forward emission.

The above experimental and numerical data are in agreement with the analysis of burn patterns on an aluminum foil taken at different locations along the beam path. At a low pulse energy (5 mJ; Fig. 4, A to C), no apparent satellite beam develops in the transverse beam plane. For a higher energy (10 mJ; Fig. 4, D to F), a satellite beam develops, and at z = 15 cm, this satellite lags the accelerating primary beam by ~1 mm. This distance is much larger than the transverse separation between the lobes of the Airy beam in the filamentation zone, therefore the satellite cannot be produced by the beam's secondary lobes. Instead, the satellite spot is most likely produced by the forward radiation from a secondary filament that has bifurcated from the primary curved filament. The 1-mm distance between the satellite spot and the dominant lobe of the beam at z = 15 cm is consistent with the data on the angularly resolved forward emission shown in Fig. 3F, as well as with the simulation results of Fig. 2D that

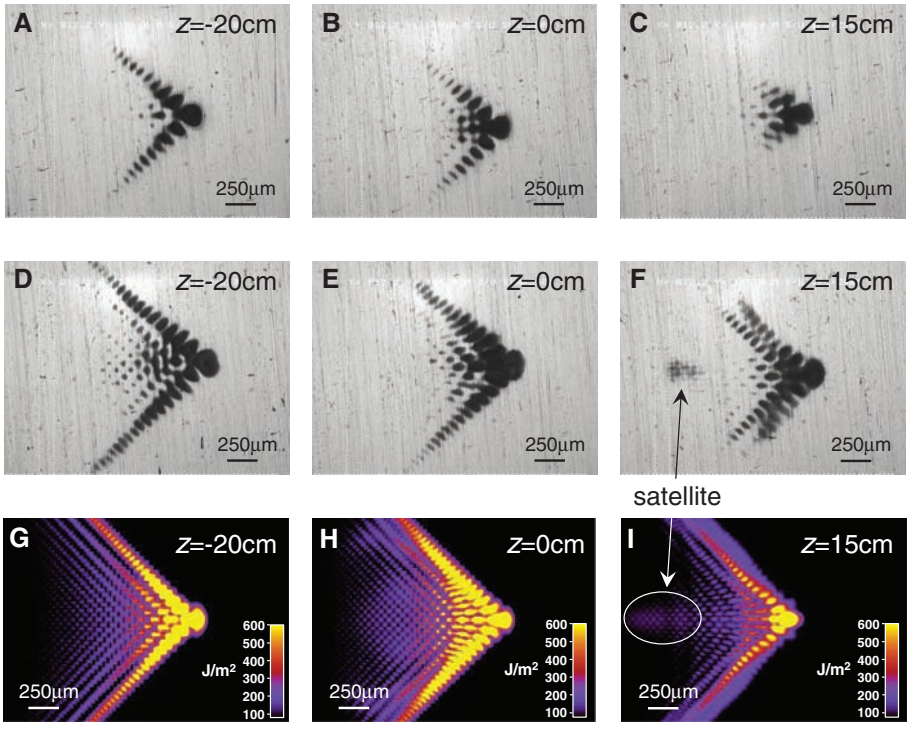

Fig. 4. Near-field beam patterns at different locations along the propagation direction. (**A** to **C**) Burn patterns on an aluminum foil for 5-mJ pulses. No apparent satellite is formed in the transverse plane during propagation. (**D** to **F**) Same as in (A) to (C) but for 10-mJ pulses. The beam undergoes a nonlinear reshaping, and a satellite spot appears that is indicated by the arrow in image F. (**G** to **I**) Numerically simulated near-field intensity profiles for 10-mJ pulses. Both the whisker-shaped ghost beam and the faint satellite are visible in (I).

shows the first branching-off event occurring at $z \approx -20$ cm. In both low- and high-energy cases, a complex nonlinear reshaping of the Airy wave packet takes place in which the high-intensity beam core develops a whiskerlike ghost beam that exhibits slightly faster acceleration compared to the primary Airy beam. The ghost beam is clearly visible in the high-intensity case. The beam reshaping features are well reproduced by the simulations that show both the whiskerlike structure and the faint satellite developing on propagation (Fig. 4, G to I).

The above observations suggest that the dominant lobe of the Airy beam acts as a "light bullet," an intense concentration of electromagnetic energy that travels along a curved trajectory and leaves a bent plasma channel behind. This wave packet is ~130 μm in diameter, 10 μm long (corresponding to the 35-fs-long pulse), and carries ~30% of the total energy of the laser pulse. Under these conditions, the wave packet's trajectory deviates from a straight line by over 2 mm, which is much larger than its size in both the transverse and longitudinal dimensions. For high pulse energies, secondary bullets bifurcate from the primary one but they quickly die out. The highly nonlinear propagation regime of the intense femtosecond Airy wave packet resembles that of a spatio-temporal soliton wave. What makes it markedly different is the fact that the Airy wave packet propagates along a curved trajectory, whereas known solitons in uniform media propagate along straight paths.

References and Notes

1. A. Braun *et al.*, *Opt. Lett.* **20**, 73 (1995).
2. Q. Luo *et al.*, *Appl. Phys. B* **82**, 105 (2006).
3. A. Proulx, A. Talebpour, S. Petit, S. L. Chin, *Opt. Commun.* **174**, 305 (2000).
4. C. D'Amico *et al.*, *Phys. Rev. Lett.* **98**, 235002 (2007).
5. C. P. Hauri *et al.*, *Appl. Phys. B* **79**, 673 (2004).
6. J. Kasparian *et al.*, *Opt. Express* **16**, 5757 (2008).
7. M. Mlejnek, E. M. Wright, J. V. Moloney, *Opt. Lett.* **23**, 382 (1998).
8. J. Kasparian *et al.*, *Science* **301**, 61 (2003).
9. A. Couairon, A. Mysyrowicz, *Phys. Rep.* **441**, 47 (2007).
10. D. Faccio *et al.*, *Phys. Rev. Lett.* **96**, 193901 (2006).
11. S. Tzortzakis *et al.*, *Opt. Lett.* **25**, 1270 (2000).
12. P. Polynkin *et al.*, *Opt. Express* **16**, 15733 (2008).
13. S. Akturk, B. Zhou, M. Franco, A. Couairon, A. Mysyrowicz, *Opt. Commun.* **282**, 129 (2009).
14. M. Châteauneuf, S. Payeur, J. Dubois, J.-C. Kieffer, *Appl. Phys. Lett.* **92**, 091104 (2008).
15. G. A. Siviloglou, J. Broky, A. Dogariu, D. N. Christodoulides, *Phys. Rev. Lett.* **99**, 213901 (2007).
16. G. A. Siviloglou, D. N. Christodoulides, *Opt. Lett.* **32**, 979 (2007).
17. G. A. Siviloglou, J. Broky, A. Dogariu, D. N. Christodoulides, *Opt. Lett.* **33**, 207 (2008).
18. M. V. Berry, N. L. Balazs, *Am. J. Phys.* **47**, 264 (1979).
19. I. M. Besieris, A. M. Shaarawi, *Opt. Lett.* **32**, 2447 (2007).
20. P. Saari, *Opt. Express* **16**, 10303 (2008).
21. M. Kolesik, J. V. Moloney, M. Mlejnek, *Phys. Rev. Lett.* **89**, 283902 (2002).
22. See supporting material on *Science* Online.
23. J. Broky, G. A. Siviloglou, A. Dogariu, D. N. Christodoulides, *Opt. Express* **16**, 12880 (2008).
24. J. Baumgartl, M. Mazilu, K. Dholakia, *Nat. Photonics* **2**, 675 (2008).

25. This work was supported by the U.S. Air Force Office of Scientific Research through grants FA9550-07-1-0010 and FA9550-07-1-0256. The contribution of G.A.S. and D.N.C. was partially supported by Lockheed Martin Corporation. We thank T.-M. O. Crust for stimulating discussions and D. Hansen and T. Milster for fabricating cubic phase masks used in the experiments.

Supporting Online Material

www.sciencemag.org/cgi/content/full/324/5924/229/DC1
Materials and Methods
SOM Text
References

9 December 2008; accepted 23 February 2009
10.1126/science.1169544

Solar Power Wires Based on Organic Photovoltaic Materials

Michael R. Lee, Robert D. Eckert, Karen Forberich, Gilles Dennler, Christoph J. Brabec, Russell A. Gaudiana*

Organic photovoltaics in a flexible wire format has potential advantages that are described in this paper. A wire format requires long-distance transport of current that can be achieved only with conventional metals, thus eliminating the use of transparent oxide semiconductors. A phase-separated, photovoltaic layer, comprising a conducting polymer and a fullerene derivative, is coated onto a thin metal wire. A second wire, coated with a silver film, serving as the counter electrode, is wrapped around the first wire. Both wires are encased in a transparent polymer cladding. Incident light is focused by the cladding onto to the photovoltaic layer even when it is completely shadowed by the counter electrode. Efficiency values of the wires range from 2.79% to 3.27%.

The use of organic and hybrid solar cells, based on nanostructured bulk heterojunction composites, represents a general approach toward flexible solar cells with reduced costs and size (*1*–*8*). The photoactive layer, as reported by Sariciftci *et al*. (*9*–*11*), consists of a conducting polymer and a solubilized fullerene derivative PCBM [(6,6)-phenyl-C_{61} butyric acid methyl ester]. These components, which are for the most part insoluble in one another, can be dissolved in a mutual solvent. When the resulting homogenous solution is coated as a thin layer on a substrate, the polymer and fullerene partially phase separate into intertwined wormlike or channel-like domains. This morphology creates an extremely high surface between the polymer phase (the electron donor) and the fullerene phase (the electron acceptor) that enhances the efficiency of electron collection.

If the cross-sectional dimension of the channels is in the range from 20 to 50 nm, excitons produced in the polymer phase, upon absorption of incident radiation, diffuse to the interface with the fullerene phase. At this interface, an electron from the excited state of the polymer is transferred to the fullerene phase. The hole, or cation, on the polymer chain, from which the electron was ejected, migrates to the secondary electrode by an electron/hole exchange mechanism between neighboring polymer chains. The electron in the fullerene phase hops from one fullerene molecule to another as it moves toward the primary electrode. The electrons flow from the primary electrode to an external load and reenter the cell via the secondary electrode. At the interface with the secondary electrode, each hole residing on the polymer chain picks up an electron, which converts it back to its ground state, thus completing the electrical circuit.

Theoretical studies have shown that the most recent generation of bulk heterojunction composites has an efficiency potential >10% for single junction devices (*12*) and 15% for dual junction (tandem) devices (*13*) that absorb in two different wavelengths, e.g., the visible and the near infrared.

One of the major difficulties with organic photovoltaics (OPV) wire technology is the thinness of the photoactive coatings, which can lead to shorting between the electrodes if their surface features exceed the combined layer thickness. Consequently, a wire core is required with a smooth surface in order to eliminate shorts resulting from large surface spikes. In addition, an n-type carrier counter electrode that is both highly conductive and optically transparent has not been reported. Even indium-tin oxide coatings with a resistivity as low as 10 ohm/cm^2 cannot transport the photocurrent generated with 1 sun irradiance over more than 10 to 15 mm without incurring electrical losses. Thus, we use one wire as the primary electrode for collecting electrons generated by the active layer, and we successively coat all three of the photocell layers, for example, the electron transport layer, the photoactive layer, and the hole transport layer, in sequence on top of one another, placing layer upon layer around the core wire. Each of the coatings

Konarka Technologies, Incorporated, Lowell, MA 01852, USA.

*To whom correspondence should be addressed. E-mail: rgaudiana@konarka.com

Curved Plasma Channel Generation Using Ultraintense Airy Beams

Pavel Polynkin, Miroslav Kolesik, Jerome V. Moloney, Georgios A. Siviloglou and Demetrios N. Christodoulides

Science **324** (5924), 229-232.
DOI: 10.1126/science.1169544